

# Antiferromagnetic Josephson junctions and the formation of spin-triplet current

Jingy Li

April 12, 2025

## 1 Abstract

This study involves Details the fabrication and analysis of superconducting-ferromagnetic-superconducting (SFS) Josephson junctions, comparing structures with and without copper layers adjacent to the antiferromagnetic chromium (Cr) spacer. The junctions were fabricated on silicon substrates via photolithography, sputtering (using Nb/Al base electrodes, Fe/Cr ferromagnetic-antiferromagnetic layers, and Au/Cu interfaces), and ion milling. Two groups were studied: one with copper layers encapsulating the Cr and one without:

"A" junctions:  $[Nb(25)/Al(2.4)]_3/Nb(20)/Cu(2)/Cr(x)/Fe(3)/Cr(x)/Cu(2)/Nb(5)/Au(10)$

"B" junctions:  $[Nb(25)/Al(2.4)]_3/Nb(20)/Cr(x)/Fe(3)/Cr(x)/Nb(5)/Au(10)$ .

Measurement at 4.2 K employed a custom SQUID setup to measure critical current ( $I_c$ ) dependence on magnetic flux, revealing Fraunhofer patterns modeled by Bessel functions for elliptical junctions. A symmetric phase shift in  $I_c$  relative to zero field was observed, though suppression during upper magnetic sweeps was absent, suggesting unresolved magnetization dynamics in the Cr/Fe layers.

The work is to demonstrate the role of spin-triplet Cooper pairs, which evade exchange field decoherence, as a potential mechanism for non-dissipative spin currents in superconducting spintronics.

## Contents

<b>1</b>	<b>Abstract</b>	<b>1</b>
<b>2</b>	<b>Fabrication</b>	<b>3</b>
2.1	Sample preparation . . . . .	3
2.2	Photolithography for setup and bottom lead deposition . . . . .	3
2.3	Sputtering . . . . .	3
2.4	SFS junctions sputtering . . . . .	6
2.5	E-beam lithography . . . . .	6

2.6	Ion milling . . . . .	6
2.7	Top Lead . . . . .	7
<b>3</b>	<b>Measurement</b>	<b>9</b>
3.1	SQUID measurement . . . . .	10
3.2	Spin triplet pairs . . . . .	11
3.3	Adding ferromagnetic and antiferromagnetic layers . . . . .	12
<b>4</b>	<b>Understanding the Suppression of Triplet Current in Josephson Junctions</b>	<b>13</b>
4.1	Adjusting the Fit Function for Cr/Fe/Cr Junctions . . . . .	13
<b>5</b>	<b>How spin triplet current form in superconducting gap</b>	<b>15</b>
<b>6</b>	<b>Derivation of Gor'kov Equations from Hamiltonian Commutators</b>	<b>17</b>
6.1	Equation of Motion for Green's Functions . . . . .	17
6.2	Operator Commutator Substitution . . . . .	17
6.3	Fourier Transform to Matsubara Frequency . . . . .	18
6.4	Anomalous Green's Function Dynamics . . . . .	18
6.5	Layer-Specific Equations . . . . .	18
6.6	Full Gor'kov System . . . . .	18
6.7	Key Physical Insights . . . . .	19
<b>7</b>	<b>Simulation</b>	<b>19</b>
<b>8</b>	<b>Special thanks</b>	<b>19</b>

## 2 Fabrication

The sample fabrication thin-layer Josephson junction takes multiple steps in clean room and sputtering chamber, as well as ion-milling and other chemical developing method to remove the unwanted layers, leaving the Josephson junction and the circuit pattern defined protected by the photoresist and lithography exposure. The following section introduce a detailed fabrication process. [2]

### 2.1 Sample preparation

A three-inch polished silicon wafer is coated with S1813 photoresist in a class 100 cleanroom using a Headway resist spinner at 5000 rpm for 50 seconds. After baking at 90°C for 2 minutes, the wafer is diced into 0.495-inch chips using an ADT wafer dicing saw. Post-dicing, the chips are labeled with a diamond scribe and cleaned by acetone rinse and a 70°C ultrasonic acetone bath for 10 minutes. The cleaning process continues with rinses in isopropanol (IPA) and deionized water (DI), followed by drying with nitrogen and cleanroom wipes. Chips are subjected to oxygen plasma etching at 300 watts for 10 minutes to remove residues. These steps prepare the chips for Josephson junction fabrication. [2]

### 2.2 Photolithography for setup and bottom lead deposition

The previously cleaned chips were first baked at 110°C to remove residual water and then placed on a Headway photo-resist spinner set at 3000 rpm for 45 seconds to spin-coat S1813-G2 photo-resist (positive photo-resist for ultraviolet light exposure) for the bottom layer. The photoresist is a light-sensitive chemical substance that can become active/inactive (depends on if it is "positive" or "negative" photo-resist) under the exposure of ultraviolet light source or electron beams (will be discussed in the next steps involving E-beam lithography) . [2]

S1813-G2 photoresist used for bottom layer is a positive resist so under the mask aligner with certain geometric shapes only the area under the glass ABM photo-mask are exposed by the ultraviolet light near wavelength 405nm and 365nm for 11 seconds. Then the samples were immersed into MF319 developer and then rinsed by DI water to create an photo-lithographically-characterized pattern for sputtering of the metals that were deposited onto the surface sample adhesive to the bare regions of the substrate. The metals deposited on top of the photo-resist was later removed with the *lift-off process* which involves immersing the sample in acetone and dissolve the hardened photo-resist along with the metal on top of it. [2]

### 2.3 Sputtering

The samples were loaded into the sputtering chamber in aluminum sample holders that has stainless steel shutter with a single square shutter that can be manually opened by a control stick from outside the sputtering chamber that allow the sample to be exposed for sputtering during the sputtering process. Before loading the sample the thorough cleaning of the holder in a solution of 1 : 3 DI water to nitric acid for 30 minutes and

rinsing afterwards with DI water. And then all parts are placed into a beaker that fill with acetone and placed in sonication bath for 5 minutes. Then this process is repeated for ethanol and DI water. The sample holder parts were dried with heat gun and placed in zipper bags to isolate from contamination. [2]

Each holders can hold two substrates and were labeled with letter indicating different group (with/without copper) and numbers for individual samples indicating the varying width of the Cr layer. The sample holders were then loaded on a plate that has vacancies of the shape of the sample holders after the sputtering chamber was baked for eight hours to evaporate any possible water molecules and then cryopumped over night to reach the base pressure of  $2 \times 10^{-8}$  torr (around  $5 \times 10^{-6}$  atm). The base pressure can be adjusted during the sputtering by using a purifier that introduce gas into the chamber. The gate valve to the cryopump can be adjusted to control the pressure so it stabilize at around  $2.3 \times 10^3$  during the sputtering. The targets for metal sputtering are cooled with water that runs through and directed to a sink.[2]

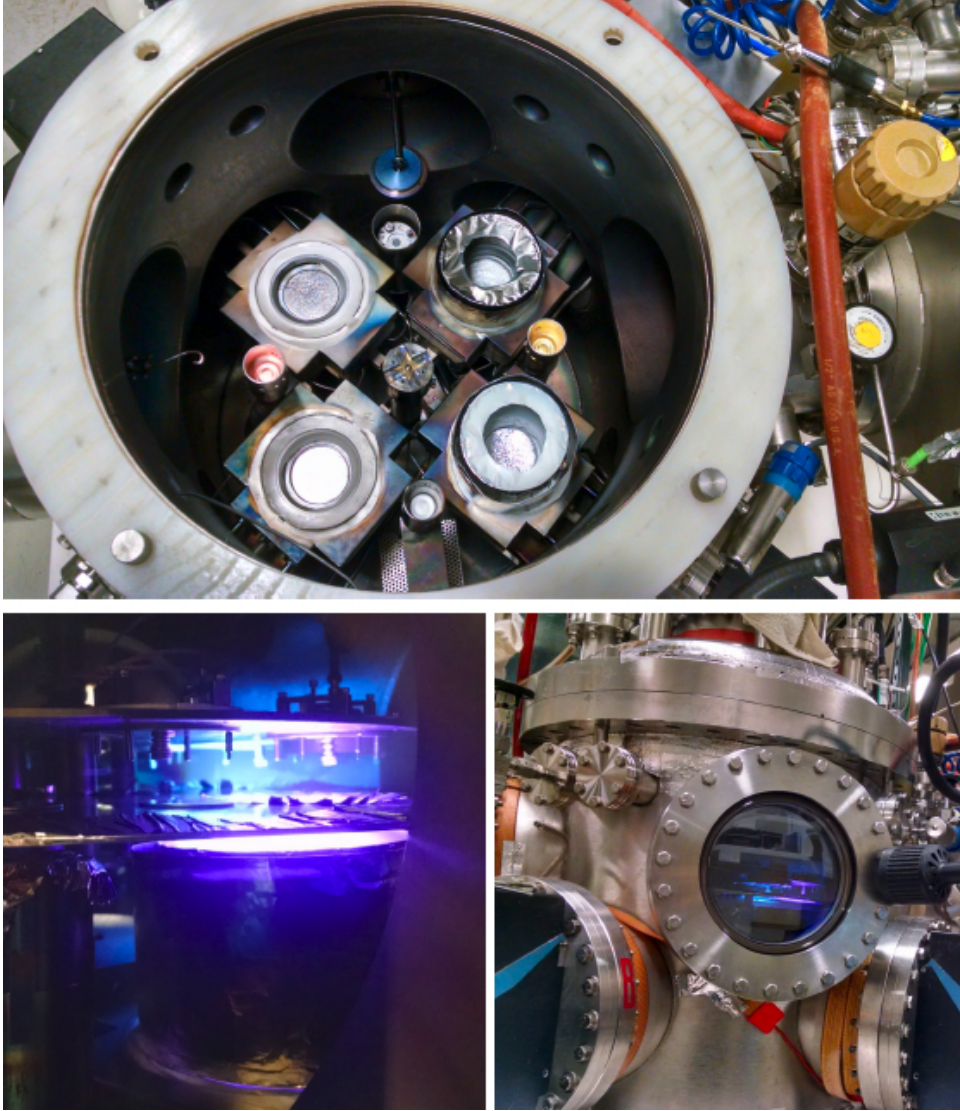


Figure 1: (top) The inside of the sputtering chamber with targets to load different pure metals for  $Ar$  plasma sputtering and deposition. (bottom left) Observation from the window outside during the sputtering run. (bottom right) Observation of ion-milling from outside during the run. The sputtering chamber contains four large DC magnetron guns with Nb, Al, Fe, and Cr targets, and three small DC magnetrons with Au, Ru, and Cu targets. A small ion mill is located at the 12 o'clock position. Foil chimney collimators are visible on Nb and Al targets. The sputtering process shows purple and blue plasma over Al and Nb targets, with the sample holder, film thickness monitor, and shutter plate wrapped in Al foil.

Sputtering of each different layers of metals require the sample holding plate to rotate and then shutter opens for the metal target to sputter. And the sputtering time for different metals are also different and had to be calibrated carefully for the layer depth that were achieved.

## 2.4 SFS junctions sputtering

There are two groups of Josephson with varying Cr width being fabricated using high-vacuum sputtering deposition. One group without copper layers outside the anti-ferromagnet chromium **Cr**. The other with copper layers.

The result comparing the franhoffer pattern of Superconducting interference measurement of coupled DC Josephson junctions (DC SQUID) is attached below in the measurement section.

## 2.5 E-beam lithography

and is dispensed with a disposable pipette directly over the chip center before the spin-coating process to avoid contamination.

Starting with previously , we bake them at 110°C to remove residual water. After cooling, each chip is placed on a , and the surface is cleaned with a nitrogen gun. Using a disposable pipette, photoresist is dispensed directly over the chip center to avoid contamination. A final plasma descum at 100 watts for 2 minutes is conducted before loading samples into holders for next round of sputtering. [2]

## 2.6 Ion milling

After the E-beam exposure, the ion milling and thermal evaporation (**configured in the same ion-milling chamber**) were used for etching away the metal layers to define Josephson junctions and depositing the  $\text{SiO}_x$  to protect the sidewalls of the remaining material and isolate the top and bottom superconducting electrodes. The E-beam resist after E-beam exposure done earlier acts as a ion-mill mask that protects everything underneath while making sure everything else is away after the ion-milling. As demonstrated in the 2, after final liftoff with Remover PG that has been warmed up to 90C for 10 minutes (could be longer if the top leads were not completely removed) and then mechanically assisted liftoff with Q-tip (brushing surface carefully with specially made tip), then again PG remover for 1 hour. In the end the sample with removed material on sidewalls were placed in DI water and blow dry with nitrogen then placed under optical microscope for examination for the pancake shaped junction. [2]

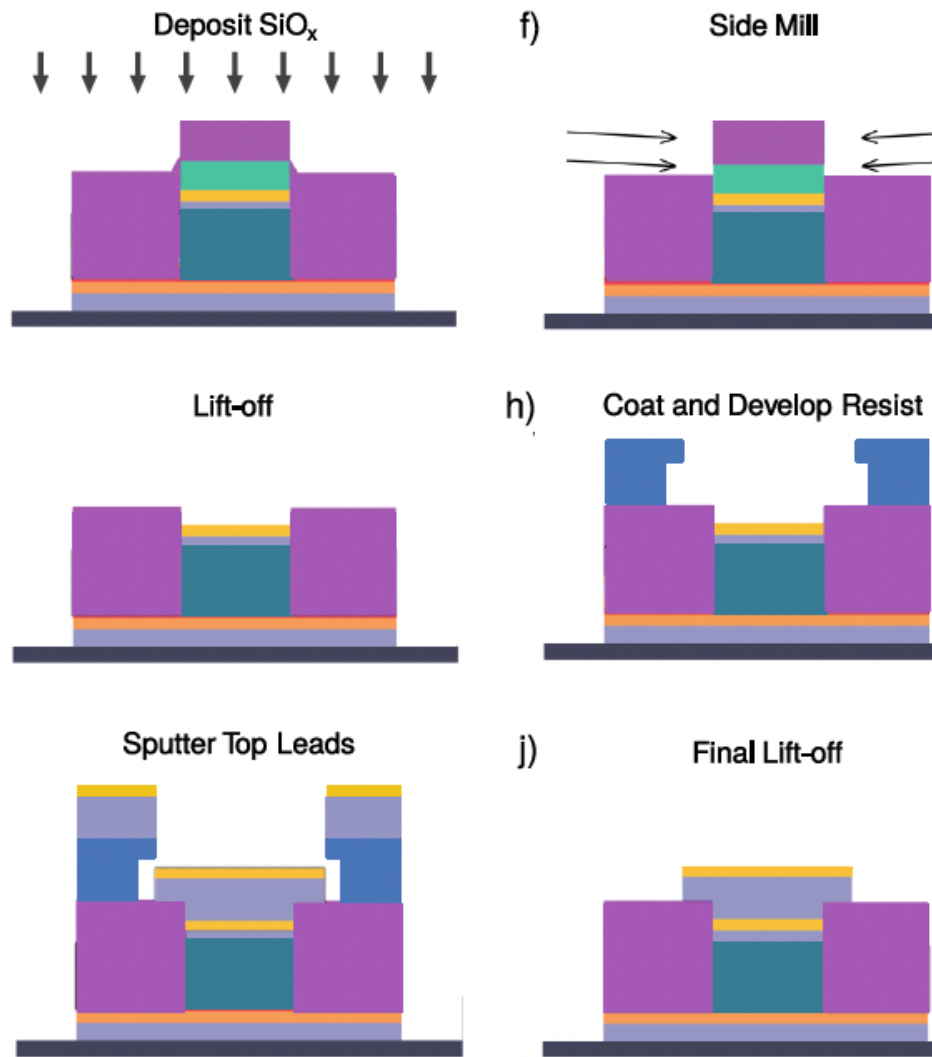


Figure 2: *Josephson junction fabrication steps: deposition, side-mill, lift-off, coat and develop resist, sputter top leads and final lift-off* : The

## 2.7 Top Lead

After this the top lead was again deposited by similar process with mask aligning photolithography and then sputtering and ion milling to make sure that the top lead Nb and Au was deposited.

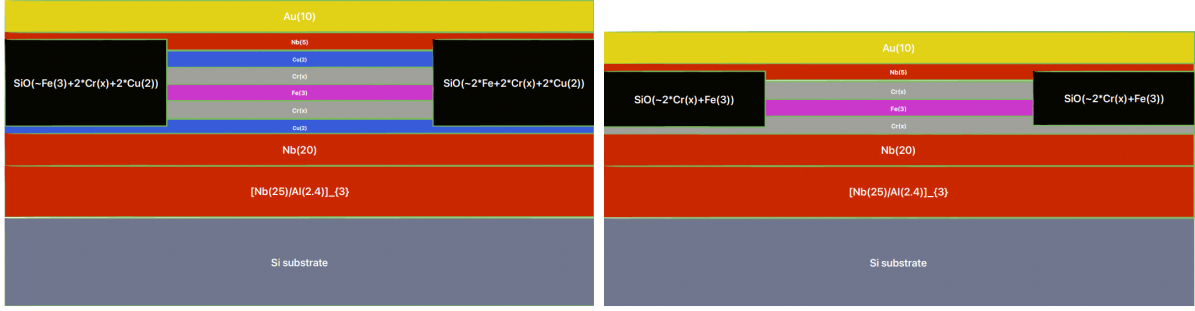


Figure 3: (a) A schematic representation of the cross-sectional structure of the set of *SF/S* Josephson with copper layer junctions. (b) Without copper layers. The ferromagnets (*Fe*) and antiferromagnets (*Cr*) are grown on a smooth superconducting Nb/Al base electrode.

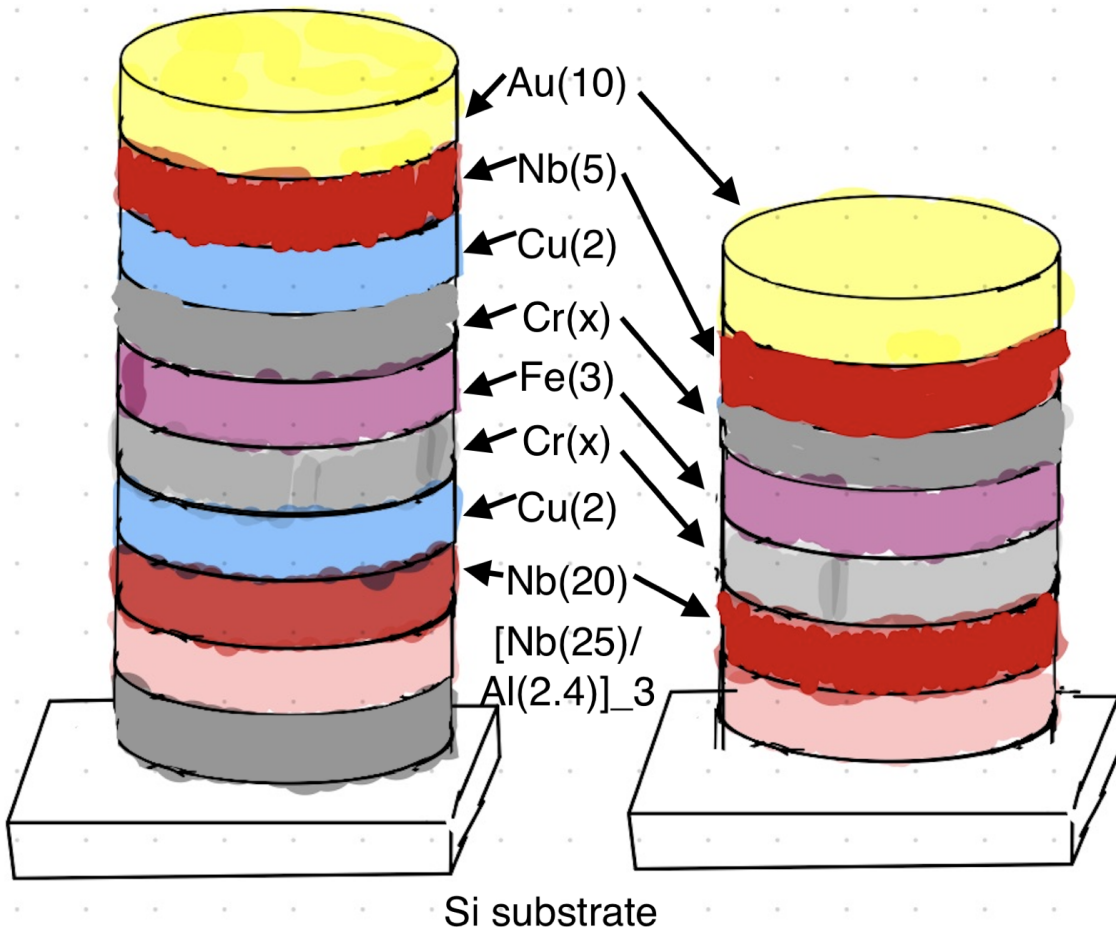


Figure 4: A more detailed and visible junction schematics as in elliptical shapes.



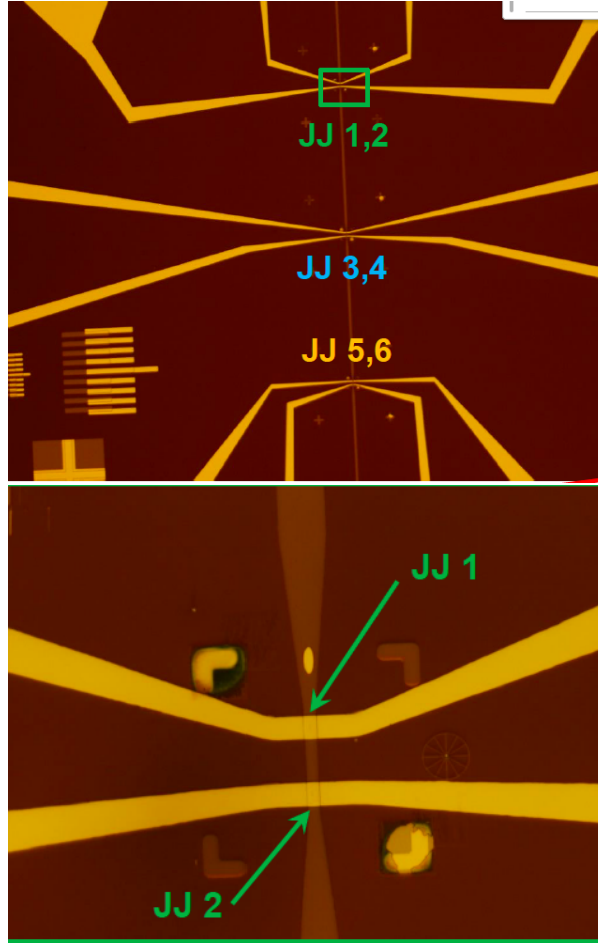


Figure 5: Ellipse shaped top-lead on the bottom lead with the top-lead josephson circuit connecting to different electrodes (square-shaped) for I-V measurement and SQUID measurement connections; Magnified ellipse-shaped top lead on the bottom lead shown as light brown, the surrounding walls are deposited by evaporating  $\text{SiO}_x$  to become adhesive to the substrate in order to prevents electrical shorts that could occur due to overlap in the metal layers.

### 3 Measurement

The measurement at 4.2K was done by immersing the sample connected to the house-made Quick Dipper I (QD-I) for I-V characteristic measurements and Quick Dipper II (QD-II) for SQUID measurement, developed by William Pratt, into the Dewar of liquid helium. The I-V characteristic curves of the Josephson junction samples were first measured quickly with the simplest four-point measurements to confirm the superconductivity and then the sample that achieve zero resistivity (flat I-V curve up until certain voltage/current ,in superconducting state) transferred to the QD-2 and connected to a RF-SQUID which consist of a single Josephson junction in a superconducting loop. [2]

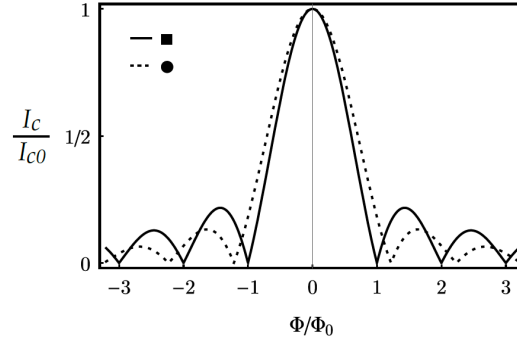


Figure 6: Fraunhofer patterns for rectangular (Sinc function, solid) and circular Josephson junctions (Airy function, dashed).

### 3.1 SQUID measurement

The Fraunhofer pattern measurement utilizes a SQUID device immersed in liquid helium at 4.2 K, with the sample mounted on a brass base and shielded from external noise using a mu-metal sheath. [2]

A superconducting solenoid applies an external magnetic field perpendicular to the SQUID loop, sweeping from  $-120\text{mT}$  to  $120\text{mT}$  in small increments. At each field step, the critical current ( $I_c$ ) is extracted from the current-voltage ( $I$ - $V$ ) characteristics using low-noise electronics and a programmable source. Initially, the samples are magnetized with a high field (up to  $\pm 150\text{ mT}$ ) to align ferromagnetic domains and eliminate trapped flux, followed by returning the system to a zero-field state. As the magnetic field is swept, the variation of  $I_c$  forms the Fraunhofer interference pattern, which reflects the critical current density dependence on the applied magnetic flux ( $\Phi$ ) from the solenoid coils perpendicular to the surface. The critical current is described by the Airy function (because of elliptical shaped junctions): [2]

$$\begin{aligned} I_s &= \int_{r=0}^R \int_{\alpha=0}^{2\pi} J_c \sin(kr \cos \alpha + \phi(0)) r dr d\alpha \\ &= 2J_c \pi R^2 \frac{J_1(kR)}{kR} \sin \phi(0), \\ I_c &= 2I_{c0} \left| \frac{J_1(\pi\Phi/\Phi_0)}{\pi\Phi/\Phi_0} \right|. \end{aligned}$$

where  $J_1$  is the first-order Bessel function,  $\Phi_0$  is the magnetic flux quantum, and  $I_{c0}$  is the maximum critical current. This pattern provides insights into the junction's magnetic alignment, uniformity, and possible asymmetries.

For the rectangular junction: (not used in our experiments, since our junctions were elliptical) [2]

$$\begin{aligned} I_s &= \int_{z=-L/2}^{L/2} \int_{y=-W/2}^{W/2} J_c \sin(kz + \phi(0)) dy dz \\ &= J_c W L \frac{\sin(kL/2)}{kL/2} \sin \phi(0) \end{aligned} \tag{1}$$

### 3.2 Spin triplet pairs

The triplet current with spin-aligned Cooper pairs immune to the exchange field of the F layer and can carry a non-dissipative spin current. Therefore becoming an interesting phenomenon for the emerging field of superconducting spintronics. From the figure 7 that is from a paper [4]

S-wave spin-triplet pairs with anti-symmetrization of overall wave function is maintained by odd-frequency pairing states [5] [4] that are recently detected majorly in the S/FL/FR/S devices where the FL and FR layers have non-collinear magnetization (one of them in-plane, one of the coupled out of plane by antiferromagnetic coupling, for example, in Nb/Ni/Cu/Co/Ru/Co/Cu/Ni/Nb devices or with synthetic antiferromagnet (SAF) formed by antiparallel coupling by a thin Ru spacer of two back to back multilayer of  $[\text{Pd}/\text{Co}]_n$  to achieve a guaranteed perpendicular magnetization of F to F'' and F'' (non-coplanar magnetization). [1]

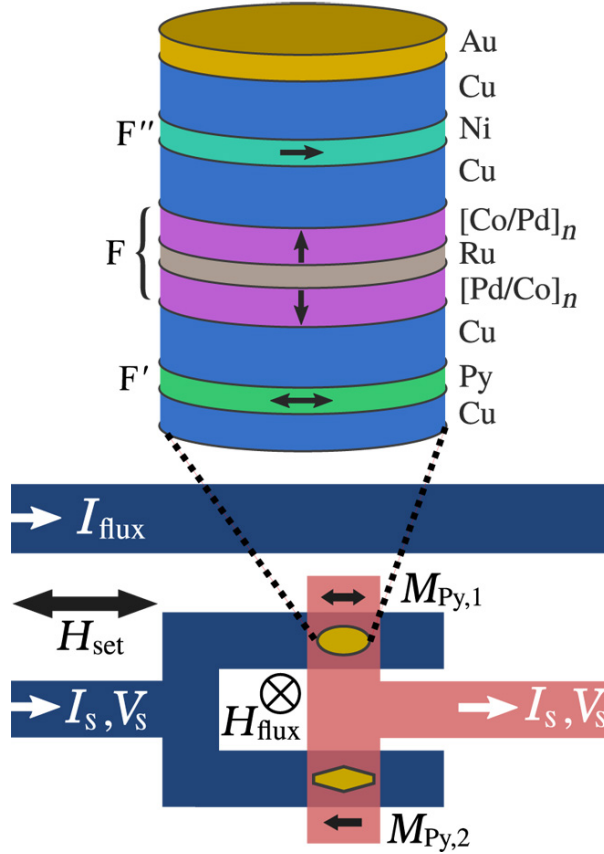


Figure 7: Top: Schematic of the central layers, featuring a synthetic antiferromagnet (SAF) with  $[\text{Pd}(0.9\text{nm})/\text{Co}(0.3\text{nm})]_n$  multilayers separated by  $\text{Ru}(0.95\text{ nm})$ . Outer F' and F'' layers (Permalloy for F' and Ni for F'') have in-plane magnetization. Junction shapes: elliptical (aspect ratio 2.0) and elongated hexagon (aspect ratio 3.0), each with a  $0.5\text{ }\mu\text{m}^2$  area. Bottom: Two junctions form a SQUID loop. An external field  $H_{\text{set}}$  controls F' and F'' magnetizations, while  $I_{\text{flux}}$  induces  $H_{\text{flux}}$ , coupling magnetic flux  $\Phi$  into the SQUID loop. Magnetizations  $M_{\text{Py},1}$  and  $M_{\text{Py},2}$  are indicated by arrows.

### 3.3 Adding ferromagnetic and antiferromagnetic layers

In the measurement of a Josephson junction coupled with a SQUID under a sweeping perpendicular-to-surface magnetic field with antiferromagnetically coupled layers, the sweeping external magnetic field revealed unresolved out-of-plane magnetization during downward sweeps (blue), and this inhomogeneity appears to break the spin-orbit coupling that suppressed the critical current. As shown in the figure below:

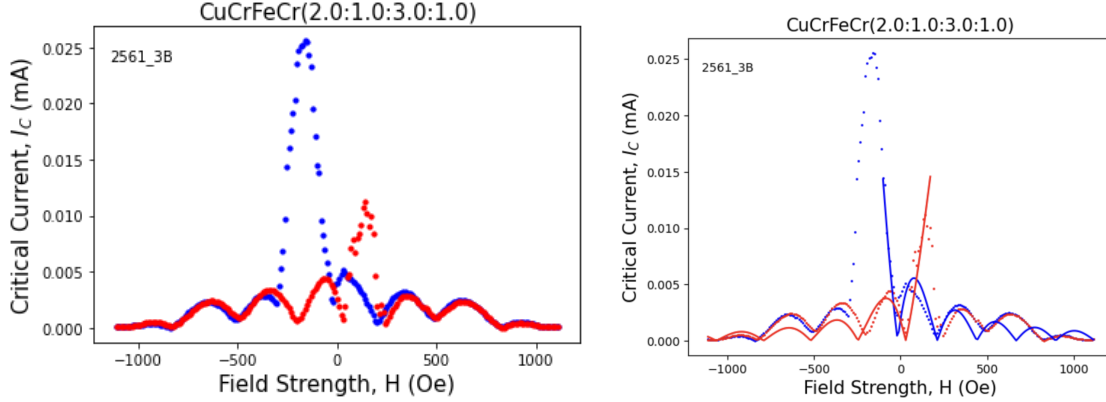


Figure 8: Antiferromagnetically coupled Josephson junction Cr/Fe/Cr measured with SQUID over the sweeping magnetic field against the critical current density. The symmetric phase shift about  $H = 0$  reflects the magnetization reversal of the Fe/Cr layers. The absence of critical current suppression during the upper sweep (positive field direction) contrasts with prior synthetic antiferromagnet (SAF)-based junctions.

The critical current density  $J_c$  versus magnetic field ( $H$ ) in Cr/Fe/Cr junctions exhibits a symmetric phase shift about  $H = 0$  (Fig. 8), consistent with the magnetization reversal of the antiferromagnetically coupled Fe layers. This symmetry arises from the spin-mixing and spin-rotation processes at the Cr/Fe interfaces, which convert singlet Cooper pairs into spin-triplet pairs. However, unlike SAF-based devices, the upper sweep ( $H > 0$ ) shows no suppression of  $J_c$ , despite expectations from prior studies.

This discrepancy may stem from unresolved magnetization dynamics in the Fe/Cr layers. During field sweeps, the Fe magnetization reversal likely occurs inhomogeneously due to spin-glass behavior at Fe/Cr interfaces (dead layers  $\sim 0.2\text{--}0.3$  nm), as inferred from vibrating sample magnetometry (VSM) and hysteretic  $J_c(H)$  profiles. Incomplete domain alignment during down-sweeping ( $H \rightarrow 0$ ) could leave residual magnetic disorder, allowing triplet pairs to persist. Spin-orbit coupling (SOC) in Nb further complicates this: while SOC scatters spin-polarized triplet pairs in the normal state ( $\xi_{\text{Nb}}^{\text{triplet}} \sim 5$  nm), the superconducting singlet gap blocks triplet coherence over longer distances ( $\xi_{\text{Nb}}^{\text{triplet}} < 30$  nm). The interplay between these effects may lead to asymmetric triplet survival during sweeps. [3]

Additionally, the lack of suppression could reflect competing mechanisms in the triplet decay envelope. In SAF-based junctions, antiparallel magnetization alignment ensures robust triplet generation, but in Cr/Fe/Cr, spin-glass interfaces introduce stochastic magnetization configurations. Quasiparticles traversing these disordered regions may retain partial spin polarization, enabling triplet currents to evade full suppression. This hy-

pothesis aligns with the paper’s observation that triplet pairs decay rapidly in Nb unless stabilized by controlled spin-mixing interfaces.

Future investigations should focus on domain-resolved magnetization measurements during field sweeps and atomistic modeling of Fe/Cr interfacial dynamics. Resolving these mechanisms could enable precise control of triplet transport for superconducting spintronic applications.

## 4 Understanding the Suppression of Triplet Current in Josephson Junctions

The suppression of spin-triplet currents in superconducting-ferromagnetic (S/F) Josephson junctions is governed by two intertwined mechanisms. Spin-orbit coupling (SOC) in the normal state of Nb disrupts triplet Cooper pairs via spin-flip scattering, drastically reducing their coherence length to  $\sim 5$  nm—an order of magnitude smaller than the singlet coherence length ( $\xi_{\text{Nb}}^{\text{singlet}} \sim 52$  nm). This decay is quantified by  $\xi_{\text{Nb}}^{\text{triplet}} \approx \frac{1}{2} (I_{\text{so}}/6)^{1/3}$ , where  $I_{\text{so}}$  is the spin-orbit scattering mean free path. Concurrently, **\*\*singlet-state blocking\*\*** in the superconducting state prevents triplet pairs from hybridizing with the s-wave singlet condensate due to incompatible spin symmetry, resulting in a complete blockade of triplet supercurrents over distances comparable to  $\xi_{\text{Nb}}^{\text{singlet}}$ . These effects are amplified in a  $S_1/F_1/S'/F_2/S_2$  junction architecture, where the central superconductor ( $S'$ )—with a lower critical temperature ( $T_{c0}$ ) than the outer electrodes ( $S_1, S_2$ )—intensifies the competition between singlet and triplet pairing. The singlet gap ( $\Delta_0$ ) in  $S'$  dominates this competition, effectively suppressing triplet propagation and underscoring the interplay between material properties and quantum coherence in superconducting spintronics.

### 4.1 Adjusting the Fit Function for Cr/Fe/Cr Junctions

The  $\text{Cr}/\text{Fe}/\text{Cr}$  Josephson junctions with and without copper layers with its **antiferromagnetic Cr layers** and **ferromagnetic Fe layers** would demonstrate spin-glass behavior at the interfaces leading to unresolved magnetization dynamics leading to the absence of suppression of the spin-triplet current in the upper sweep of the critical current  $I_c$  during magnetic field sweeps in SQUID measurement.

The spin-glass behavior at Fe/Cr interfaces introduces stochastic magnetization configurations[5], which can leave residual magnetic disorder called **magnetic inhomogeneity** during field sweeps. This allows triplet pairs to persist, even in the presence of SOC. The symmetric phase shift in  $I_c(H)$  suggests that triplet pairs dominate the critical current, with minimal singlet contribution.

Because of this magnetic inhomogeneity a new fitting function needs to be taken into consideration : [3][5]

$$I_c(\Phi) = I_{c0} \left| \frac{J_1(\pi(\Phi - \delta)/\Phi_0)}{\pi(\Phi - \delta)/\Phi_0} \right| e^{-d_{\text{Nb}}/\xi_{\text{triplet}}},$$

The critical current behavior in the junction can be modeled using a framework that incorporates several key physical parameters and functions. At its core, the maximum critical current,  $I_{c0}$ , is modulated by a first-order Bessel function ( $J_1$ ), which replaces

the conventional sinc function to account for the elliptical geometry of the junctions. The magnetic flux quantum,  $\Phi_0 = h/2e \approx 2.07 \times 10^{-15}$  Wb, governs the flux periodicity, while a phase shift term ( $\delta$ ), arising from magnetic hysteresis at the Fe/Cr spin-glass interfaces, introduces symmetric deviations in  $I_c(H)$  around  $H = 0$ . The suppression of triplet superconducting pairs due to spin-orbit coupling (SOC) in the normal state of Nb is captured by an exponential decay term  $e^{-d_{\text{Nb}}/\xi_{\text{triplet}}}$ , where  $d_{\text{Nb}}$  is the Nb layer thickness and  $\xi_{\text{triplet}}$  (typically 3.2~5.7 nm) represents the triplet coherence length, which is significantly shorter than the singlet coherence length. For experimental fitting, initial parameters should be carefully chosen:  $I_{c0}$  is extracted directly from the measured critical current,  $\delta$  is initially set to zero and refined based on observed hysteresis symmetry,  $\xi_{\text{triplet}}$  is informed by literature values, and  $d_{\text{Nb}}$  corresponds to the known Nb layer thickness in the device. Together, these elements provide a comprehensive model linking junction geometry, material properties, and magnetic history to the observed critical current behavior. When the fitting function

As shown in the figure 9, the fitting was much better than previously with considering predominant triplet current near 0 field and predominant singlet current with higher field, considering the spin-glass behavior arisen from the magnetic inhomogeneity, suggesting there indeed exist non-resolved magnetization at the interface.

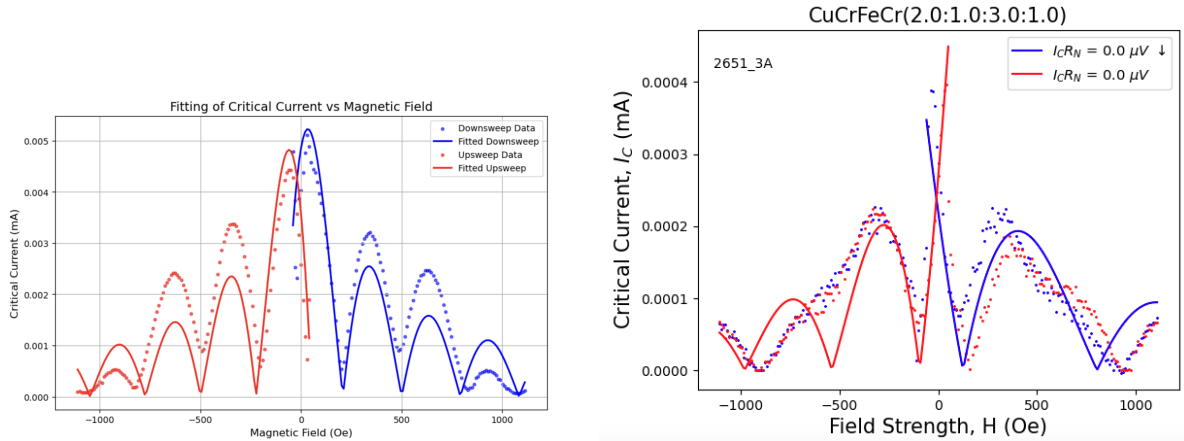


Figure 9: The well-fitted spin-triplet current with the implementation of gradient search separately for up-sweep and down-sweep, it proves that the phase transition for the up-sweep and down-sweep is also symmetric. On the left the fitting shows difference in  $I_{c0}$  when magnetization swept upward and downward. Meanwhile the right figure without the copper layer shows that the same  $I_{c0}$ , which would be interesting to investigate the copper layer's row in spin-rotation at the interfaces.

From the plot in 9 it does seem that without the copper layer (B group, without the copper layer) was able to have more symmetric Fraunhofer pattern and smaller (suppressed) critical current (current suppressed) for both up-sweeping and down-sweeping indicating spin-orbit coupling was not broken through out the whole external magnetic field induced magnetization.

It seems that  $Cu$  spacer of  $2nm$  in A group mitigates this suppression by spatially separating the superconducting and magnetic layers, preserving the coherence of Cooper pairs near the interface, which cause the critical current to be larger. It also enables

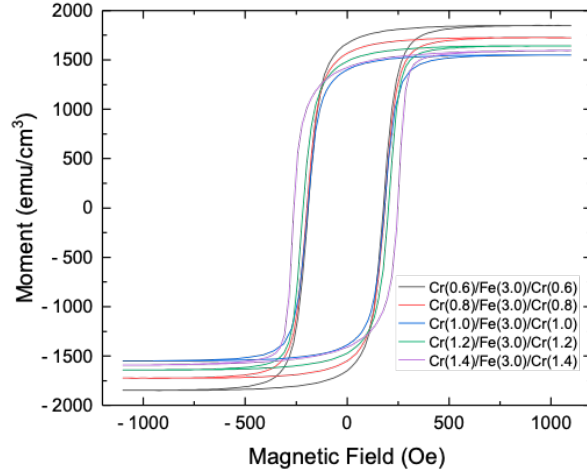


Figure 10: Measurement of magnetization sweeping observed Hysteresis for Cr/Fe magnetization bevaivor under sweeping magnetic field

spin-rotation by allowing the spin-triplet to not be filtered out by the direct coupling to *Nb* which is known to be a singlet superconductor (its energy gap  $\Delta_0$  does not have enough energy states to host spin-triplet pairs). The triplet pair then propagate a longer range than just singlet current and are measured.

There are several papers already mentioning the  $0 - \pi$  transition at near the ferromagnetic interface, as well as the relation between the critical current density and the spacer depth (basically the propagation length) of the spin-triplet current without it being broken by magnetization when coupling to ferromagnetic junction. This can be indirectly seen from the experiment also done at Birge group earlier on replacing the Cu spacer completely with Pd that enhances spin-triplet current coherent length,

The hysteresis of the plot 10 shows a rectangular shaped

## 5 How spin triplet current form in superconducting gap

From the paper [Jeon2018EnhancedSpin] it is shown that the order parameter in superconductor and ferromagnetic metal (FM) are different, therefore when spin-singlet or spin-triplet pair propagate through the interface, only those matching the energy state in the FM could propagate through, this is called the "proximity effect", or explained by Andreev reflection. Spin-singlet pairs are suppressed in FMs due to spin polarization mismatch, while spin-triplet pairs (with equal-spin components) propagate because they align with the FM's majority spins. Singlet Andreev reflection is blocked in half-metallic FMs (because there are no opposite-spin states). Triplet Andreev reflection enables same-spin retro-reflection, sustaining spin currents into the FM.

The signature of spin-triplet current is long relaxation time and longer coherence length (or less diffusive scattering with the impurities).

The band-gap formed by cooper pair condensation, which open-gap energy states near the Fermi energy level.



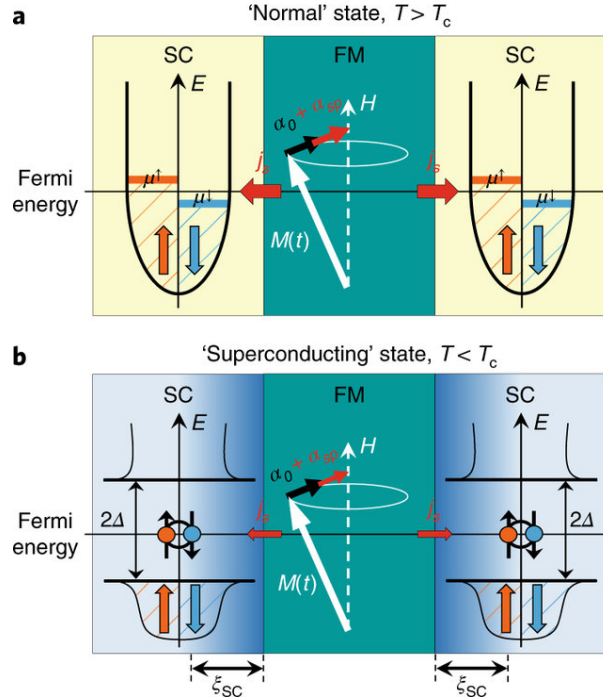


Figure 11: Enter Caption

## RCSJ model and Landau-Lifshitz-Gilbert (LLG) equation for magnetisation dynamics

The SC/F Josephson junction can be considered as a shunted resistor-capacitor which observes harmonic oscillator equation:

$$\begin{aligned}
 I_c + I_J + I_R &= I \\
 \frac{\Phi_0}{2\pi} C \ddot{\delta} + I_c \sin(\delta) + \frac{\Phi_0}{2\pi R} \dot{\delta} &= I \\
 \frac{\Phi_0}{2\pi} C \ddot{\delta} + \frac{\Phi_0}{2\pi R} \dot{\delta} &= I - I_c \sin(\delta) \\
 \ddot{\delta} + \frac{1}{RC} \dot{\delta} &= \left( \frac{2\pi}{C\Phi_0} \right) (I - I_c \sin(\delta))
 \end{aligned} \tag{2}$$

This can be simply demonstrated by the coupled capacitor, resistor and Josephson junction depending on the relative comparison between the current in the junction with critical current, and the order parameter level. Essentially from the above equations we can use rather simplified interpretation of an underdamped and an overdamped harmonic oscillator to explain the behavior of the Josephson junction,

The behavior of a Josephson junction depends on whether the current  $I$  is below or above the critical current  $I_c$ , as this governs the generation of quasi-particles and the nature of the superconducting current. When  $I < I_c$ , the current flows entirely as a supercurrent, described by  $I_s = I_c \sin \phi$ , where  $\phi$  is the phase difference across the junction. In this regime, the phase remains static ( $\dot{\phi} = 0$ ), resulting in zero voltage ( $V = 0$ ) and suppressing quasi-particle generation, as no energy dissipation occurs. However, when  $I > I_c$ , the supercurrent breaks down, and a voltage develops across the junction



due to a time-varying phase ( $\dot{\phi} \neq 0$ ), given by  $V = \frac{\hbar}{2e}\dot{\phi}$ . This voltage activates quasi-particle currents ( $I_R = V/R_n$ ) through normal electron transport and leads to energy dissipation via Joule heating. Additionally, Cooper pairs can break into quasi-particles when  $eV \geq 2\Delta$ , where  $\Delta$  is the superconducting gap. The transition from  $I < I_c$  to  $I > I_c$  qualitatively changes the phase dynamics: below  $I_c$ ,  $\phi$  is static, while above  $I_c$ ,  $\phi(t)$  oscillates continuously, reflecting a resistive state dominated by quasi-particles.

## 6 Derivation of Gor'kov Equations from Hamiltonian Commutators

The derivation connects the commutators of the Hamiltonian to the Gor'kov equations (S5-S9) for the  $S_1/F_1/S'/F_2/S_2$  Josephson junction. We systematically transform operator dynamics into Green's function equations through the following steps:

### 6.1 Equation of Motion for Green's Functions

The time evolution of operators in imaginary time  $\tau$  follows the Liouville equation:

$$i\frac{\partial\Psi}{\partial\tau} = [\widehat{H}, \Psi]. \quad (3)$$

For the normal Green's function in the  $S'$  layer:

$$G_{\uparrow\uparrow}(\mathbf{p}; \tau_1, \tau_2) = -\langle T_\tau \hat{\phi}_{\mathbf{p},\uparrow}(\tau_1) \hat{\phi}_{\mathbf{p},\uparrow}^\dagger(\tau_2) \rangle, \quad (4)$$

differentiating with respect to  $\tau_1$  gives:

$$i\frac{\partial G_{\uparrow\uparrow}}{\partial\tau_1} = -\langle T_\tau [\widehat{H}, \hat{\phi}_{\mathbf{p},\uparrow}(\tau_1)] \hat{\phi}_{\mathbf{p},\uparrow}^\dagger(\tau_2) \rangle. \quad (5)$$

### 6.2 Operator Commutator Substitution

Using the provided commutator for  $\hat{\phi}_{\mathbf{p},\uparrow}$ :

$$[\widehat{H}, \hat{\phi}_{\mathbf{p},\uparrow}] = -\xi\hat{\phi}_{\mathbf{p},\uparrow} + \Delta_0\hat{\phi}_{-\mathbf{p},\downarrow}^\dagger - t_2\hat{\psi}_{\mathbf{p},\uparrow} - t_3\hat{\psi}_{\mathbf{p},\uparrow}, \quad (6)$$

we substitute into the equation of motion:

$$i\frac{\partial G}{\partial\tau_1} = \xi G - \Delta_0\langle T_\tau \hat{\phi}_{-\mathbf{p},\downarrow}^\dagger \hat{\phi}_{\mathbf{p},\uparrow}^\dagger \rangle + t_2\langle T_\tau \hat{\psi}_{\mathbf{p},\uparrow} \hat{\phi}_{\mathbf{p},\uparrow}^\dagger \rangle + t_3\langle T_\tau \hat{\psi}_{\mathbf{p},\uparrow} \hat{\phi}_{\mathbf{p},\uparrow}^\dagger \rangle. \quad (7)$$

Recognizing the Green's functions:

$$\langle T_\tau \hat{\phi}_{-\mathbf{p},\downarrow}^\dagger \hat{\phi}_{\mathbf{p},\uparrow}^\dagger \rangle = F_{\uparrow\downarrow}^\dagger, \quad \langle T_\tau \hat{\psi}_{\mathbf{p},\uparrow} \hat{\phi}_{\mathbf{p},\uparrow}^\dagger \rangle = -E_{\uparrow\uparrow}^\psi. \quad (8)$$

### 6.3 Fourier Transform to Matsubara Frequency

Assuming time-translation invariance and Fourier transforming:

$$G(\mathbf{p}; i\omega) = \int_0^\beta d\tau e^{i\omega\tau} G(\mathbf{p}; \tau), \quad (9)$$

where  $\omega = (2n + 1)\pi/\beta$ . The derivative becomes  $-i\omega$ :

$$-i\omega G = \xi G - \Delta_0 F^\dagger + t_2 E^\psi + t_3 E^{\tilde{\psi}}. \quad (10)$$

Rearranging terms yields the first Gor'kov equation:

$$(i\omega - \xi)G + i\Delta_0 \sigma_y F^\dagger - t_2 E^\psi - t_3 E^{\tilde{\psi}} = I. \quad (11)$$

### 6.4 Anomalous Green's Function Dynamics

For the anomalous Green's function  $F^\dagger$ :

$$[\widehat{H}, \hat{\phi}_{-\mathbf{p},\downarrow}^\dagger] = \xi \hat{\phi}_{-\mathbf{p},\downarrow}^\dagger + \Delta_0^* \hat{\phi}_{\mathbf{p},\uparrow} + t_2 \hat{\psi}_{-\mathbf{p},\downarrow}^\dagger + t_3 \hat{\tilde{\psi}}_{-\mathbf{p},\downarrow}^\dagger, \quad (12)$$

leading to the second Gor'kov equation:

$$(i\omega + \xi)F^\dagger - i\Delta_0^* \sigma_y G + t_2 F^{\psi\dagger} + t_3 F^{\tilde{\psi}\dagger} = 0. \quad (13)$$

### 6.5 Layer-Specific Equations

For the  $F_1$  layer, from the commutator of  $\hat{\psi}_{\mathbf{p},\uparrow}$ :

$$(i\omega - P_\uparrow)E^\psi - t_1 E^\eta - t_2 G = 0, \quad (14)$$

with  $P_\uparrow = \text{diag}(\xi, \infty)$ . Similarly for  $S_1$ :

$$(i\omega - \hat{C}^{(1)})E^\eta + i\Delta_1 \sigma_y F^{\eta\dagger} - t_1 E^\psi = 0. \quad (15)$$

### 6.6 Full Gor'kov System

The complete set of equations becomes:

$$\begin{cases} (i\omega - \xi)G + i\Delta_0 \sigma_y F^\dagger - t_2 E^\psi - t_3 E^{\tilde{\psi}} = I \\ (i\omega + \xi)F^\dagger - i\Delta_0^* \sigma_y G + t_2 F^{\psi\dagger} + t_3 F^{\tilde{\psi}\dagger} = 0 \end{cases} \quad (\text{S5}) \quad (16)$$

$$\begin{cases} (i\omega - P_\uparrow)E^\psi - t_1 E^\eta - t_2 G = 0 \\ (i\omega + P_\downarrow)F^{\psi\dagger} + t_1 F^{\eta\dagger} + t_2 F^\dagger = 0 \end{cases} \quad (\text{S6}) \quad (17)$$

$$\begin{cases} (i\omega - \hat{C}^{(1)})E^\eta + i\Delta_1 \sigma_y F^{\eta\dagger} - t_1 E^\psi = 0 \\ (i\omega + \hat{C}^{(1)})F^{\eta\dagger} - i\Delta_1^* \sigma_y E^\eta + t_1 F^{\psi\dagger} = 0 \end{cases} \quad (\text{S8}) \quad (18)$$

## 6.7 Key Physical Insights

The  $\Delta_0 \sigma_y F^\dagger$  term mediates conversion between triplet correlations from  $F_{1,2}$  and the singlet condensate in  $S'$ . The spin-polarized tunneling ( $E^\psi$ ) depends on  $t_2$  and  $P_\uparrow$ , reflecting spin-selective transport. The hierarchical structure requires perturbative expansion in  $t_i$  to isolate Josephson current contributions, demonstrating how singlet superconductivity in  $S'$  suppresses spin-triplet supercurrents through the  $b|\Delta_0|^2$  term in the current density expression:

$$j_y = 8e\nu_0 t_1^2 t_2^2 t_3^2 t_4^2 |\Delta_1|^2 T (h_1 \sin \theta_1) (h_2 \sin \theta_2) (a - b|\Delta_0|^2) \sin \varphi. \quad (19)$$

## 7 Simulation

### Short conclusion

The experiment itself had demonstrated quite interesting result, with unconventional spin-rotation existing at the  $F/AF/S$  interface, with very limited samples being able to be measured. Future measurement on spin polarizations or energy band near the interface would be very insightful for looking for new mechanism for cooper pair bound state to exist in both spin-singlet and spin-triplet state.

## 8 Special thanks

Special thanks to Prof.Dr.Birge for important project instructions and special thanks for Mr. Josh Willard and Mr. Robert M. Klaes for clean room training and special thanks for Dr.Alex Madden for helping with explaining the important insight of theory behind , and clean room and Microfabrication Scientist Dr. Bi Baokang, CMP specialist Dr. Reza Loloee for training me the clean room specialisation and the usage of other fabrication devices and methods. Also thanks to MSU Condensed Matter Physics department for allowin me to use the clean room facilities and measurment devices to be able to achieve the result demonstrated in this report.

## References

- [1] E. C. Gingrich et al. “Controllable  $0-\pi$  Josephson junctions containing a ferromagnetic spin valve”. In: *Nature Physics* 12.6 (2016), pp. 564–567. ISSN: 1745-2481. DOI: 10.1038/nphys3681. URL: <https://doi.org/10.1038/nphys3681>.
- [2] III Glick Joseph Allen. “Controllable Josephson Junctions with Ferromagnetic Barriers”. PhD Thesis. Michigan State University, 2017, pp. xvi + 235. ISBN: 9780355524666. DOI: 10.25335/409d-rm18.
- [3] Sachio Komori et al. “Spin-orbit coupling suppression and singlet-state blocking of spin-triplet Cooper pairs”. In: *Science Advances* 7.3 (2021), eabe0128. DOI: 10.1126/sciadv.abe0128. eprint: <https://www.science.org/doi/pdf/10.1126/sciadv.abe0128>. URL: <https://www.science.org/doi/abs/10.1126/sciadv.abe0128>.

- [4] D. Korucu, Reza Loloee, and Norman O. Birge. “Demonstration of  $0 \rightarrow \pi$  transition in Josephson junctions containing unbalanced synthetic antiferromagnets”. In: *Applied Physics Letters* 124.24 (June 2024), p. 242603. ISSN: 0003-6951. DOI: 10.1063/5.0215364. eprint: [https://pubs.aip.org/aip/apl/article-pdf/doi/10.1063/5.0215364/19993199/242603\\\_1\\\_5.0215364.pdf](https://pubs.aip.org/aip/apl/article-pdf/doi/10.1063/5.0215364/19993199/242603\_1\_5.0215364.pdf). URL: <https://doi.org/10.1063/5.0215364>.
- [5] Sergey Mironov et al. “Spin-orbit coupling suppression and singlet-state blocking of spin-triplet Cooper pairs”. In: *Science Advances* 7.3 (2021), eabe0128. DOI: 10.1126/sciadv.abe0128. URL: <https://advances.sciencemag.org/content/7/3/eabe0128>.